ORGANIC CHEMISTRY FRONTIERS

RESEARCH ARTICLE

View Article Online
View Journal | View Issue

Cite this: *Org. Chem. Front.*, 2024, **11**, 6495

Anomalous magnetic behaviour induced by a structural phase transition with anisotropic thermal expansion in a spirodiradical†

Takuya Kanetomo, * Daigo Matsunaga, Shinichi Ogawa and Masaya Enomoto *

Received 19th June 2024,
Accepted 23rd September 2024

DOI: 10.1039/d4qo01098a

rsc.li/frontiers-organic

The compound 2,2′,7,7′-tetra(*tert*-butyl)-9,9′(10*H*,10′*H*)spirobigermaacridine-10,10′-dioxyl (**1-Ge**) exhibits a decrease in the magnetic moment at 252 K; its magnetic moment decreases upon heating, contrary to the expected entropy gain. Structural analyses revealed anisotropic thermal expansion, with negative thermal expansion along the *b*-axis, and a structural phase transition occurring at the same temperature as that for the observed specific magnetic behaviour. This structural phase transition enables a dimer, comprising two acridine moieties, to shift toward the overlap of the two N–O sites. Although their slight misalignment suggests ferromagnetic coupling, contrary to the theoretical results, **1-Ge** exhibited an abrupt magnetic decrease across a low- to high-temperature boundary. This finding indicates the presence of a neatly overlapping configuration with strong antiferromagnetic coupling as a metastable phase in the crystal.

Introduction

Organic radicals, characterized by organic compounds with unpaired electrons, are widely employed in spin trapping,[1] spin labeling,[2] dynamic nuclear polarization,[3] organic catalysts[4] and photochromic materials.[5] They have also attracted considerable attention in molecular magnetic materials such as ferromagnets,[6] paramagnetic ligands[7] and spin transition (ST) materials.[8–11] In particular, the ST phenomenon is of significant interest for the application of magnetic materials based on pure organic substances, as it occurs around room temperature and/or involves a thermal hysteresis loop; for example, 1,3,5-trithia-2,4,6-triazapentalenyl,[8a] 3′-methylbiphenyl-3,5-diyl bis(*tert*-butyl nitroxide)[9a] and 2-azaadamantane *N*-oxyl,[9b] as shown in Scheme 1a–c, respectively. This ST behaviour is mainly driven by the equilibrium between dimerization and dissociation, and its manifestation in the solid state requires thermal bistability. Most studies indicate that the radical dimers dissociate into radical monomers upon heating owing to entropy gain, and this shift in the equilibrium leads to an increase in the magnetic moment.

Despite the typically unfavourable entropy, studies have reported a decrease in the magnetic moment upon heating, known as a reverse spin transition (rST). The rST behaviour is observed in several metal complexes with Co^{2+} and Fe^{2+} ions as a metal centre.[12,13] Many cases of rST in metal complexes are attributed to changes in the angular momentum induced by first-order phase transitions, such as order–disorder transitions in the ligands. In contrast, organic radicals have negligible angular-momentum contributions compared to metal ions; as a result, there have been no reports of rST behaviour based on the mechanism known for metal complexes. In organic radicals, a decrease in magnetization with increasing temperature has been observed in examples such as the Blatter radical cationic salt (Scheme 1d)[14] and charge-transfer complexes

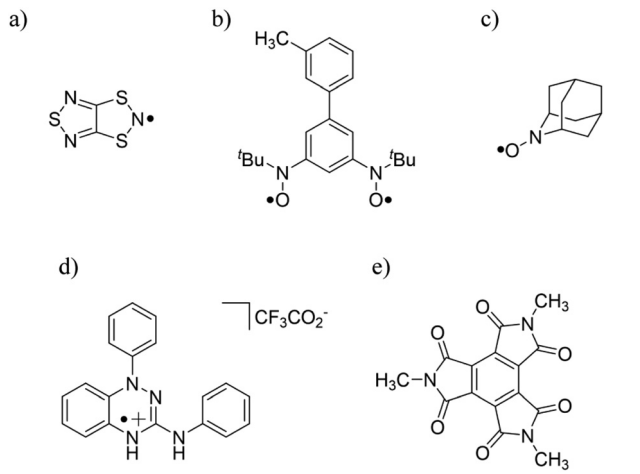

Scheme 1 (a–c) Normal and (d and e) reverse ST materials. Note that (e) is shown in the neutral state.

Tokyo University of Science, 1-3 Kagurazaka, Shinjuku-ku, Tokyo 162-8601, Japan. E-mail: kanetomo@rs.tus.ac.jp

†Electronic supplementary information (ESI) available. CCDC 2348900–2348902. For ESI and crystallographic data in CIF or other electronic format see DOI: https://doi.org/10.1039/d4qo01098a

based on the benzenetriimide derivative (Scheme 1e).[15] In these cases, the mechanism involves a change in exchange coupling from ferromagnetic (FM) to antiferromagnetic (AFM), triggered by first-order phase transitions. The normal ST in organic radicals involves a simple separation between the adjacent radical sites on heating, namely, the transition from a magnetically coupled state to a magnetically isolated state. Based on this, the manifestation of rST in organic radicals would necessitate a transition from a magnetically isolated state to a magnetically coupled state as the underlying mechanism.

Recently, we reported on the spiro-centre dependent intramolecular spin–spin interactions in spiro-based diradicals (Fig. 1a; **1-X**, X = C, Si and Ge).[16,17] While **1-C** and **1-Si** exhibited only magnetic behaviour based on spin–spin interactions below 300 K, **1-Ge** showed not only the above interaction behaviour below 100 K but also a sharp decrease in $\chi_m T$ at 252 K (Fig. 1b). This decrease process is reproducible (Fig. 1b), and there is no thermal hysteresis loop. Previous studies have noted only the occurrence of unique magnetic behaviour.[17] Therefore, in this study, to elucidate the mechanism underlying the magnetic behaviour, we conducted variable-temperature single-crystal X-ray diffraction (VT-SCXRD), electron spin resonance (VT-ESR) spectroscopy and thermal analysis of the polycrystalline sample **1-Ge**. Furthermore, we employed theoretical calculations based on density functional theory (DFT). Through these analyses, we have proposed the mechanism for the anomalous magnetic behaviour observed in **1-Ge**. The abrupt magnetic decrease across the low- to high-temperature boundary occurs as magnetically isolated spirodiradical molecules undergo the structural phase transition, resulting in a partially magnetically coupled state with strong AFM contributions.

Experimental

Materials and methods

Compound **1-Ge** was prepared following a reported procedure.[17] The magnetic measurements (Fig. 1b) have been reported in our previous study.[17] For reference, the measurement conditions are provided. The magnetic susceptibilities were measured under a static field of 0.5 T on a Quantum Design MPMS-XL7AC SQUID magnetometer equipped with a 7 T coil. The temperature scan rate was *ca.* 2 K min^{-1} in a temperature range of 2–300 K (1st heating) and 160–300 K (1st cooling and 2nd heating). VT-ESR spectra were recorded on a Bruker EMXnano X-band (9.6 GHz) spectrometer. The temperature scan rate was *ca.* 5 K min^{-1} in the range of 230–270 K. Differential scanning calorimetry (DSC) was carried out using a Bruker DSC3500. The temperature scan rate was 5 K min^{-1} in the range of 230–275 K.

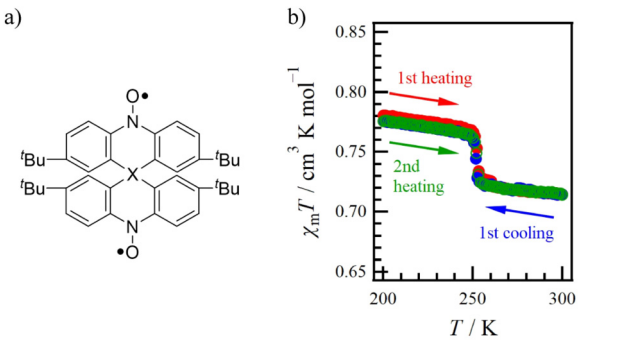

Fig. 1 (a) Molecular structure of **1-X** (X = C, Si and Ge). (b) Temperature dependence of $\chi_m T$ for **1-Ge**. Red, blue and green represent the 1st heating, 1st cooling and 2nd heating processes, respectively.[17]

Single-crystal X-ray diffraction

The X-ray diffraction data of **1-Ge** at 220, 250 and 280 K were collected on a Bruker D8 QUEST diffractometer (Mo Kα radiation: λ = 0.71073 Å). X-ray data analyses were carried out using the SHELXT[18] and SHELXL[19] programs operated with the Olex2 interface.[20] All the hydrogen atoms were refined as "riding". The thermal displacement parameters of the non-hydrogen atoms were refined anisotropically. The occupancy (occ) factor was optimized to be 0.75/0.25 and 0.72/0.28 for major/minor components at 250 and 280 K, respectively, of the C14/C15/C16 atoms in the *tert*-butyl group. In addition, the occ factor was also optimized to be 0.68/0.32 and 0.76/0.24 for major/minor components at 250 and 280 K, respectively, of the C39 atom in the *tert*-butyl group. The CCDC numbers of **1-Ge** at 220, 250 and 280 K are 2348900–2348902,† respectively. Furthermore, we performed measurements, only to confirm the cell parameters, in the range of 90–300 K. The results are summarized in Table S1.† The coefficients of thermal expansion (CTE; α_l and α_V) were calculated from the data provided in Table S1† and Fig. 3.

Theoretical calculations

The DFT calculations were performed using the Gaussian09 program.[21] The energies of the triplet (T) and broken-symmetry singlet (BS) states were calculated at the UB3LYP/6-311+G(2d,p) level. The structural parameters were obtained from the crystallographic data. Notably, when calculating the intermolecular contact, the dihydroacridine moiety, which is not involved in the contacts, and the *tert*-butyl groups were replaced by methyl groups, to reduce computational costs. In addition, the magnetic interactions through the intermolecular H-bonding (C–H···O) were carried out not only with UB3LYP but also with UM06-2X, the latter to account for the effects of H-bonding. Intermolecular interaction constants dependent on the parallel shift between the NO dimers were calculated at the UB3LYP/6-31+G(d,p) level to reduce the computational cost.

Results and discussion

VT-ESR spectroscopy

To validate the anomalous magnetic behaviour observed in the $\chi_m T$ *vs.* T plot (Fig. 1b), VT-ESR spectroscopy was conducted

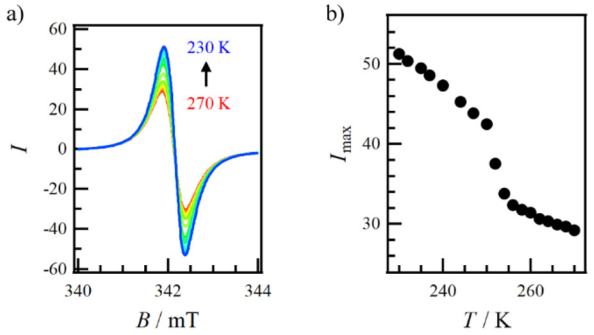

Fig. 2 (a) VT-ESR spectroscopy results within the range of 230–270 K and (b) temperature dependence of the maximum intensity (I_{max}).

on polycrystalline **1-Ge** within the range of 230–270 K (Fig. 2a). The signals can be observed across all temperatures, with no variation in *g*-values and the peak-to-peak line width. The signal intensity (I) increased upon cooling. Fig. 2b shows a plot of the maximum signal intensity (I_{max}) *vs.* T, which shows an abrupt change at 252 K. This behaviour supports the anomalous magnetic behaviour observed in the $\chi_m T$ *vs.* T plot.

Temperature dependence of crystal structures

The crystal structure of **1-Ge** has been reported in a previous study (93 K).[17] In this study, SCXRD was performed at 220, 250 and 280 K (Fig. S1†). The temperature-dependent cell parameters (a, b, c, β and V) are listed in Table 1. The crystal structures at all the measured temperatures were isomorphous (monoclinic, $P2_1/n$). Notably, the temperature-dependent cell parameters (Table S1† and Fig. 3 and S2†) revealed two significant findings: (i) a discontinuous change and (ii) negative thermal expansion (NTE). The former was clearly observed at about 250 K for parameters a and b. The DSC plot exhibits thermal peaks at 255 (upon heating) and 252 K (upon cooling), indicating that the discontinuous change corresponds to a structural phase transition (Fig. S3†). In addition, there is a gap of 3 K between the critical temperatures for cooling and heating processes, indicating a thermal hysteresis loop. However, this hysteresis is not observed in the $\chi_m T$ *vs.* T plots (Fig. 1b). This finding may be due to the difference in the sweep rate between the DSC (5 K min^{-1}) and $\chi_m T$ (2 K min^{-1}) measurements. This transition temperature corresponds to the critical temperature (252 K), suggesting a relationship between these phenomena. NTE was observed only for parameter b, whereas a, c and V exhibited positive thermal expansion (PTE). To evaluate the anisotropic thermal expansion, the coefficient of thermal expansion (CTE) values of the length (α_l; l = a, b and c) and volume (α_V) were estimated. In Fig. 3, the blue and red lines represent the fitting results before and after the structural phase transition, respectively. In the LTP (90–220 K), the CTE values of α_a, α_b, α_c and α_V were estimated to be +130, −26, +56 and +160 × 10^{-6} K^{-1}, respectively. In contrast, the CTE values in the HTP (250–300 K) were +150, −6.0, +130 and +280 × 10^{-6} K^{-1}. The α_a, α_c and α_V of both the LTP and HTP exhibit the typical PTE behaviour of molecular materials.[22] However,

Table 1 Selected crystallographic data for **1-Ge** at 93,[a] 220, 250 and 280 K

T/K	93[a]	220	250	280
Formula	$C_{40}H_{48}GeN_2O_2$			
F_w	661.39			
Crystal system	Monoclinic			
Space group	$P2_1/n$			
a/Å	12.3869(3)	12.6135(4)	13.1487(6)	13.2143(6)
b/Å	25.3893(5)	25.2804(8)	24.5633(11)	24.5170(11)
c/Å	11.2881(3)	11.3788(3)	11.5008(5)	11.5348(5)
β/°	105.385(3)	105.3610(10)	106.667(2)	106.632(2)
V/Å^3	3422.83(15)	3498.79(18)	3558.4(3)	3580.6(3)
Z	4			
d_{calcd}/g cm^{-3}	1.283	1.256	1.235	1.227
μ(Mo Kα)/mm^{-1}	0.932	0.912	0.896	0.891
$R(F)^b$ ($I > 2\sigma(I)$)	0.0308	0.0415	0.0439	0.0449
$R_w(F^2)^c$ (all data)	0.0834	0.0925	0.0919	0.0961
Goodness-of-fit	1.037	1.032	1.014	1.018

[a] Ref. 17. [b] $R = \sum||F_o| - |F_c||/\sum|F_o|$. [c] $R_w = [\sum w|F_o^2 - F_c^2|^2/\sum w(F_o^2)^2]^{1/2}$.

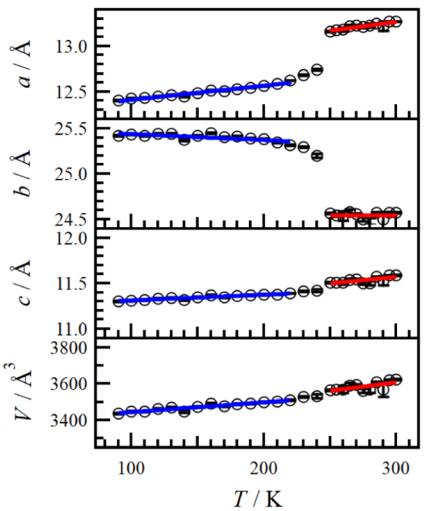

Fig. 3 Temperature dependence of cell parameters a, b, c and V (black open circles). The red and blue lines represent the fitting lines before and after the structural phase transition, respectively.

α_b shows NTE in both the HTP and LTP, with the value in the HTP being small, similar to inorganic materials.[22]

The intramolecular structural parameters measured at 220, 250 and 280 K are summarized in Table S2.† Although minor changes in the spiro-skeleton and N–O and Ge–C bonds were detected with increasing temperature, no discontinuous changes were observed. In contrast, the two *tert*-butyl (^{t}Bu) groups (including C13 and C37 atoms) changed from an ordered state in the LTP to a disordered state in the HTP. This order–disorder change can be attributed to an increase in the void space upon heating. Compound **1-Ge** exhibits two types of dimeric motif: (i) an assembly of two planar acridine units through π···π and electrostatic interactions (Fig. 4a–d and S4, Table S3†) and (ii) an assembly of the curved acridine and ^{t}Bu moiety through CH···π interactions (Fig. S5 and Table S4†). Based on these two dimeric motifs, **1-Ge** forms a non-covalent

1-D chain structure along the *a*-axis (Fig. S6†). In the crystal structure at 220 K, the three remaining ^{t}Bu groups (C13, C17 and C37), which do not participate in dimer (ii), engage in interchain contacts (Table S5†). Among them, two ^{t}Bu groups (C17 and C37) exhibit intermolecular CH···π and ^{t}Bu···^{t}Bu interactions, whereas the ^{t}Bu group (C13) only exhibits intermolecular ^{t}Bu···^{t}Bu interactions. These findings suggest that the observed order–disorder change is due to the increase in the void space around the ^{t}Bu groups (C13) upon heating.

Dimer (i) plays a key role in the structural phase transition and NTE. This dimer can be formed by aligning the planar acridine moiety on the *ab* plane, with two acridines stacked along the *c*-axis. In the LTP (220 K; Fig. 4a and b), the conformation of the two N2–O2 sites is off-centre, with one N2–O2 site positioned above the neighbouring C21 atom (Table S3†). Furthermore, the O2···C8* distance of 3.132(4) Å (Fig. 5a) is smaller than the sum of van der Waals (vdW) radii (C/O: 3.22 Å),[23] indicating strong electrostatic interaction (H-bonding formation). In contrast, the two N–O sites in the HTP (280 K) almost overlap (Fig. 4c, d and Table S3†). The O2···C8* distance is 3.080(4) Å (Fig. 5b), enhancing the electrostatic interaction. The electrostatic interactions can be explained based on the polarized structure of the two N–O sites. The N–O dimer can form from resonance structures (Scheme 2a), leading to the ground singlet state (Scheme 2b).[9] The dimeric motif at 280 K exhibited the arrangement shown in Scheme 1c. The N2···O2* distance of 3.270(6) Å is close to the sum of vdW radii (N/O: 3.07 Å),[23] suggesting weak electrostatic interactions between the two N2–O2 sites. Dimer (i) in the HTP exhibits strong and weak electrostatic interactions (the O2···C8* contact and N–O dimer). Namely, during the structural phase transition, these interactions become more pronounced, leading to a slipping motion toward the overlap of the N2–O2 sites. Locally, this slipping motion results in contraction along the *b*-axis and elongation along the *a*-axis (Fig. 4a and c). Furthermore, the interface distance between the two acridine rings in the dimer along the *c*-axis decreased from 3.442 Å (220 K, LTP) to 3.371 Å (280 K, HTP). These local changes suggest NTE along the *b*- and *c*-axes and PTE along the *a*-axis. The crystal structure is predominantly governed by CH···π and ^{t}Bu···^{t}Bu interactions, which typically exhibit PTE. Owing to the competition with these factors, **1-Ge** demonstrates NTE only along the *b*-axis.

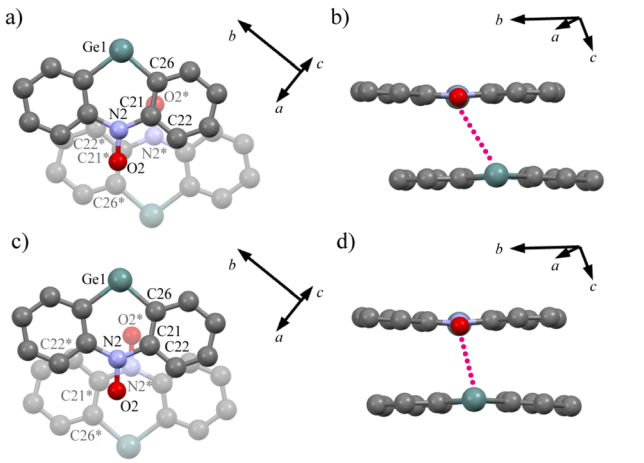

Fig. 4 (a–d) Dimer structures at (a and b) 220 K and (c and d) 280 K. For clarity, the ^{t}Bu groups, H atoms, and acridine units (including N1) are omitted. The (a and c) top- and (b and d) side-views of the dimer. The symmetric code of * is 2 − *x*, 1 − *y*, 1 − *z*. The purple supplementary dashed lines indicate the linking of two N–O sites.

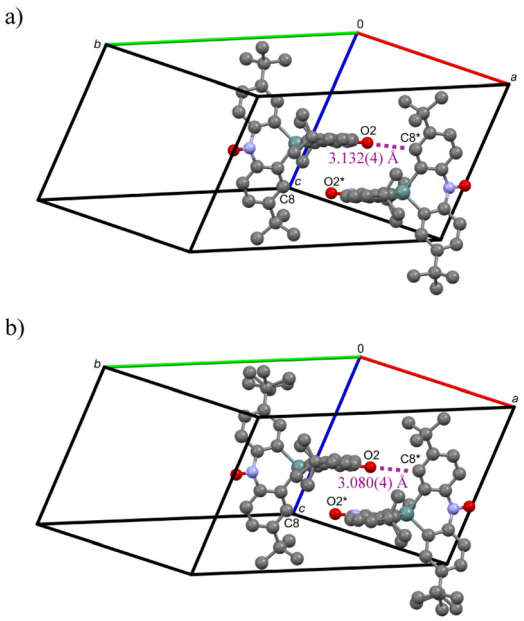

Fig. 5 The intermolecular C···O contacts of dimer (i) at (a) 220 and (b) 280 K. The symmetric code of * is 2 − *x*, 1 − *y*, 1 − *z*. H atoms are omitted.

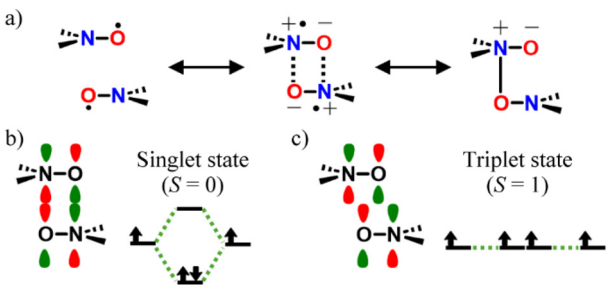

Scheme 2 (a) Resonance structures of the through-space dimerization between two N–O sites. (b and c) Two types of conformations for the N–O dimers, leading to the (b) singlet and (c) triplet states.

Theoretical calculations

DFT calculations of the HTP for **1-Ge** were conducted using crystallographic data (280 K, HTP). The intramolecular interactions were evaluated, and the T and BS energy states are listed in Table S6.† The exchange coupling constant $2J/k_B$, defined by $\hat{H} = -2JS_A \cdot S_B$, of **1-Ge** at 280 K was determined to be +13.23 K using Yamaguchi's equation,[24] which is slightly

smaller than the value at 93 K ($2J/k_B$ = +13.81 K).[17] This suggests that no significant alteration occurred in the intramolecular interactions associated with the structural phase transition. Subsequently, the intermolecular interactions associated with dimer (i) were calculated. The calculated spin density maps and energy states of the T and BS states at 280 K are shown in Fig. S7 and Table S7.† At 93 K (LTP), the intermolecular exchange coupling ($2J'/k_B$) exhibited AFM coupling with −4.62 K,[17] while at 280 K (HTP), it showed FM coupling with +50.78 K. The difference in these interactions can be attributed to the arrangement of singly occupied molecular orbitals (SOMOs) in each acridine ring. In the LTP, the N2–O2 site was positioned over the C21 atom of the adjacent molecule (Fig. 4a). The C21 atom has small negative spin density based on the spin polarization,[25] and it is positioned above the centre of the N–O site (Scheme 3a). On the other hand, in the HTP, the two N2–O2 sites overlapped (Fig. 4b and Scheme 2c). This arrangement positioned the SOMO of one N–O site above the node at the other N–O site, resulting in no overlap between the two SOMOs (Fig. S8†). These configurations show the orthogonal state, resulting in an FM interaction (Scheme 3b).[26] Consequently, the intermolecular spin–spin couplings in the LTP and HTP are the AFM and FM interactions, respectively.

Mechanism of the manifestation for the anomalous magnetic behaviour

The causes of the anomalous magnetic behaviour observed in **1-Ge** are discussed on the basis of (i) intramolecular magnetic interactions, (ii) the *g*-value and (iii) intermolecular magnetic interactions.

First, regarding (i) intramolecular interactions, a qualitative explanation can be given by the changes from FM to AFM interactions or from strong FM to weak FM interactions before and after the structural phase transition. However, theoretical calculations negate the former. As for the latter, the difference in the interactions is small, with +13.81 K for the LTP and +13.23 K for the HTP. When these interactions were applied to a simple two spin-1/2 system to compare the differences in $\chi_m T$, the experimental value was not reproduced (Fig. S9†). The difference in $\chi_m T$ between the LTP and HTP near the structural transition temperature is about 0.04 cm^3 K mol^{-1}, and reproducing this difference using only intramolecular interactions would require a change in the $2J/k_B$ of more than 30 K. In **1-Ge**, strengthening the LTP side is the only option, but this would lead to inconsistencies in the magnetic behaviour at low temperature. It is therefore not appropriate to explain the magnetic behaviour of **1-Ge** in terms of intramolecular interactions.

Next, regarding (ii) the *g*-value, both qualitative and quantitative explanations are possible if the HTP has a lower *g*-value than the LTP due to the structural phase transition. Referring to the difference in $\chi_m T$ (0.04 cm^3 K mol^{-1}) around the transition temperature, if the *g*-value of the LTP is assumed to be 2.0 (0.750 cm^3 K mol^{-1}), then the *g*-value of the HTP would need to decrease to about 1.95 (0.713 cm^3 K mol^{-1}) to reproduce this. However, the ESR results did not show such a significant change in the *g*-value (Fig. 2). Therefore, changes in the *g*-value cannot account for the decrease in the magnetic moment observed in **1-Ge**.

Finally, regarding (iii) intermolecular interactions, similar to intramolecular interactions, the magnetic behaviour of **1-Ge** can be explained if a change from AFM to FM interactions is observed. However, theoretical results suggest a change in interactions from AFM (LTP) to FM (HTP) due to the slipping motion associated with the structural phase transition. This implies an increase in magnetic moments, which does not reproduce the experimental results. In addition, since the CH···O contact is significant in the HTP, as shown in Fig. 5, theoretical calculations were carried out to investigate the spin–spin interaction mediated by this contact, resulting in $2J'/k_B$ = −0.865 K (Fig. S10 and Table S8†). This result was found to be too small to explain the anomalous magnetic behaviour observed in **1-Ge**. Therefore, intermolecular interactions should also be considered unsuitable for explaining the unique magnetic behaviour of **1-Ge**. Nevertheless, there is a possibility that AFM contributions could arise in the HTP based on the relationship between the stacking form and the spin–spin interactions in the N–O dimer (Scheme 2b and c). It has already been shown that the HTP has the intermolecular FM contribution. Here, if the stacking in the HTP is slightly glided to the configuration where the N–O sites overlap (Scheme 2b), it shows the AFM contribution. In fact, unsubstituted 9,9′(10*H*,10′*H*)spirobiacridine-10,10′-dioxyl (**2-C**) has an N–O dimer structure (Scheme 3c) and exhibits the intermolecular AFM interaction of −40.76 K derived from the DFT calculations.[27,28] Here, using the model from the 'theoretical calculations' for intermolecular interactions, we calculated the interactions $2J'$ when the configuration between the N–O dimers is glided in parallel. The results are shown in Fig. 6 and Table S9.† In Fig. 6, the negative direction of *d* indicates that the molecules are approaching each other in parallel,

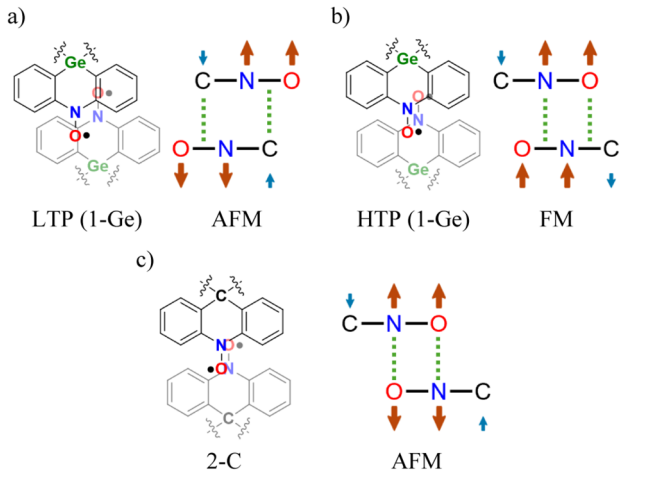

Scheme 3 Spin arrangement corresponding to the dimeric motif in (a) the LTP and (b) HTP of **1-Ge** and (c) **2-C**. Arrows on the structural formula denote the spin polarization mechanism. The *tert*-butyl groups are omitted for clarity in (a) and (b).

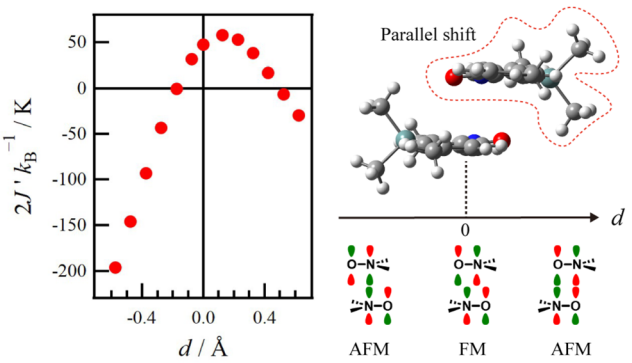

Fig. 6 Intermolecular interaction constants $2J'/k_B$ dependent on the parallel shift between the NO dimers.

while the positive direction indicates that they are moving apart in parallel. Although not explicitly shown in the calculations, the former direction corresponds to an increase in the electrostatic interaction between CH···O as shown in Fig. 5b, and the latter direction corresponds to a decrease in this interaction. From Fig. 6, it can be seen that parallel glides in either direction result in head-to-tail (positive shift) or tail-to-tail (negative shift) alignments, leading to AFM contributions. The magnitude of these contributions can be significant, for example, a displacement of about −0.4 Å resulting in the AFM interaction of about −150 K. In practice, the increase in AFM contributions is expected to shorten the distance between the N–O dimers. The AFM interactions from the overlap of SOMOs are strongly dependent on the distance between the two N–O sites.[29] For confirmation, we also calculated the intermolecular exchange coupling ($2J'$) with varying interplanar distances (d') based on the HTP structure (Table S10 and Fig. S11†). As a result, the vertical shift can play an important role in determining the magnitude of the interaction, although it does not cause the interaction to change from FM to AFM.

Consequently, we propose that the HTP in **1-Ge** includes the neatly overlapping phase form as a metastable component. The minor component contributes to the AFM interactions, leading to the anomalous magnetic decrease across the low- to high-temperature boundary in **1-Ge**. This mixing could potentially manifest as long-period structures; however, the current data do not provide insight into such phenomena. Further high-resolution structural analysis is required to provide experimental evidence.

Spiro-centre dependence of the anomalous magnetic behaviour

Although **1-X** (X = C, Si and Ge) has a similar molecular structure, the anomalous magnetic behaviour was only observed in **1-Ge**. The abrupt magnetic decrease upon heating is triggered by the structural phase transition with the anisotropic thermal expansion. It is important to compete with the NTE and PTE contributions, which are accompanied by the electrostatic interactions (O2···C8* and two N–O sites) and the dispersion force (CH···π and ^{t}Bu···^{t}Bu), respectively. While **1-C** does not have the arrangement of acridine moieties like that of dimer (i), **1-Si** has a structure similar to **1-Ge**. The reason why the Si derivative did not exhibit the anomalous magnetic behaviour is the reduction of the strong electrostatic interactions in dimer (i). The relevant distances in **1-Si** at 93 K are 3.241(1) and 3.444(1) Å, which are larger than that of **1-Ge** (3.138(2) Å at 93 K). The formation of the close dimer (i) is necessary for the NTE contribution, and therefore it is assumed that the slightly distant dimer observed in **1-Si** does not allow the structural phase transition to occur. In addition, why the electrostatic interaction in dimer (i) is weaker in **1-Si** compared to **1-Ge** can be understood by the fact that although the Ge atom is a higher period element than the Si atom, it is less likely to acquire a positive charge.[30] This tendency makes the negative charge of the surrounding carbons in Ge slightly less than in Si, which is why **1-Ge** stabilizes the strong electrostatic interaction in dimer (i).

It has already been mentioned that **2-C** forms dimer (i), but this was not observed in **1-C**, where bulky substituents (^{t}Bu) were introduced. It has been previously reported that steric effects due to such substituents can be an important factor in dimerization.[28] Compound **2-C** does not show the anomalous magnetic behaviour. This can be attributed to the absence of contacts that could compete with the intermolecular interactions responsible for dimer (i) formation. Compound **1-Ge** has not only both dimer (i) and dimer (ii) but also numerous intermolecular contacts between the ^{t}Bu groups. In contrast, **2-C** shows primarily dimer (i) with few other contacts. It is therefore assumed that **2-C** was not able to establish structural bistability and did not undergo the structural phase transition.

Based on these findings, it can be concluded that the control of intermolecular contacts, influenced by substituents and the spiro centre, is crucial for the induction of the key structural phase transition responsible for the abrupt magnetic decrease across the low-to-high temperature boundary in spirodiradicals.

Conclusions

Spirodiradical **1-Ge** exhibited a decrease in the magnetic moment at 252 K, triggered by a structural phase transition involving anisotropic thermal expansion, with only the *b*-axis exhibiting NTE. This structural phase transition can be attributed to the dimerization of two acridines with two types of electrostatic interactions: (i) H-bonding between the O2···C8* atoms and (ii) N–O dimerization. The former contributed significantly to the occurrence of the dimerization, while the latter played a crucial role in determining the spin–spin interactions. Based on the interplay between the decrease in the magnetic moment and the structural phase transition, we have proposed the presence of AFM contributions as a metastable component in the HTP of **1-Ge**, leading to the anomalous magnetic behaviour. To detect the presence of AFM dimers among the predominantly FM dimers in the HTP phase, further high-precision measurements, along with structural organic chem-

istry approaches through chemical modifications, will be required. Enhancing our understanding of this unique abrupt magnetic decrease upon heating, which has been poorly studied in organic radicals, will significantly contribute to the development of pure organic magnetic materials.

Data availability

The data supporting this article have been included as part of the ESI.† Crystallographic data for **1-Ge** have been deposited at the CCDC under numbers 2348900–2348902.†

Conflicts of interest

There are no conflicts to declare.

Acknowledgements

This study was financially supported by KAKENHI (JSPS, 24K17661).

References

1 (*a*) E. G. Janzen, Spin trapping, *Acc. Chem. Res.*, 1971, **4**, 31–40; (*b*) M. J. Davies, Detection and characterisation of radicals using electron paramagnetic resonance (EPR) spin trapping and related methods, *Methods*, 2016, **109**, 21–30.

2 (*a*) J. F. W. Keana, Newer aspects of the synthesis and chemistry of nitroxide spin labels, *Chem. Rev.*, 1978, **78**, 37–64; (*b*) A. Bonucci, O. Ouari, B. Guigliarelli, V. Belle and E. Mileo, In-Cell EPR: Progress towards Structural Studies Inside Cells, *ChemBioChem*, 2020, **21**, 451–460.

3 (*a*) O. Haze, B. Corzilius, A. A. Smith, R. G. Griffin and T. M. Swager, Water-Soluble Narrow-Line Radicals for Dynamic Nuclear Polarization, *J. Am. Chem. Soc.*, 2012, **134**, 14287–14290; (*b*) D. Wisser, G. Karthikeyan, A. Lund, G. Casano, H. Karoui, M. Yulikov, G. Menzildjian, A. C. Pinon, A. Purea, F. Engelke, S. R. Chaudhari, D. Kubicki, A. J. Rossini, I. B. Moroz, D. Gajan, C. Copéret, G. Jeschke, M. Lelli, L. Emsley, A. Lesage and O. Ouari, BDPA-Nitroxide Biradicals Tailored for Efficient Dynamic Nuclear Polarization Enhanced Solid-State NMR at Magnetic Fields up to 21.1 T, *J. Am. Chem. Soc.*, 2018, **140**, 13340–13349.

4 (*a*) L. Li, R. Matsuda, I. Tanaka, H. Sato, P. Kanoo, H. J. Jeon, M. L. Foo, A. Wakamiya, Y. Murata and S. Kitagawa, A Crystalline Porous Coordination Polymer Decorated with Nitroxyl Radicals Catalyzes Aerobic Oxidation of Alcohols, *J. Am. Chem. Soc.*, 2014, **136**, 7543–7546; (*b*) P. Qu, M. Kuepfert, S. Jockusch and M. Weck, Compartmentalized Nanoreactors for One-Pot Redox-Driven Transformations, *ACS Catal.*, 2019, **9**, 2701–2706.

5 (*a*) R. Dessauer, *Photochemistry, History, and Commercial Applications of Hexaarylbiimidazoles*, Elsevier, 2006; (*b*) A. Tokunaga, L. M. Uriarte, K. Mutoh, E. Fron, J. Hofkens, M. Sliwa and J. Abe, Photochromic Reaction by Red Light via Triplet Fusion Upconversion, *J. Am. Chem. Soc.*, 2019, **141**, 17744–17753.

6 (*a*) M. Kinoshita, P. Turek, M. Tamura, K. Nozawa, D. Shiomi, Y. Nakazawa, M. Ishikawa, M. Takahashi, K. Awaga, T. Inabe and Y. Maruyama, An Organic Radical Ferromagnet, *Chem. Lett.*, 1991, **20**, 1225–1228; (*b*) E. Jin, M. Asada, Q. Xu, S. Dalapati, M. A. Addicoat, M. A. Brady, H. Xu, T. Nakamura, T. Heine, Q. Chen and D. Jiang, Two-dimensional sp^2 carbon–conjugated covalent organic frameworks, *Science*, 2017, **357**, 673–676.

7 (*a*) I. Ratera and J. Veciana, Playing with organic radicals as building blocks for functional molecular materials, *Chem. Soc. Rev.*, 2012, **41**, 303–349; (*b*) T. Kanetomo, T. Yoshitake and T. Ishida, Strongest Ferromagnetic Coupling in Designed Gadolinium(III)–Nitroxide Coordination Compounds, *Inorg. Chem.*, 2016, **55**, 8140–8146; (*c*) H.-D. Li, S.-G. Wu and M.-L. Tong, Lanthanide–radical single-molecule magnets: current status and future challenges, *Chem. Commun.*, 2023, **59**, 6159–5170.

8 (*a*) W. Fujita and K. Awaga, Room-Temperature Magnetic Bistability in Organic Radical Crystals, *Science*, 1999, **286**, 261–262; (*b*) C. P. Constantinides, A. A. Berezin, G. A. Zissimou, M. Manoli, G. M. Leitus, M. Bendikov, M. R. Probert, J. M. Rawson and P. A. Koutentis, A Magnetostructural Investigation of an Abrupt Spin Transition for 1-Phenyl-3-trifluoromethyl-1,4-dihydrobenzo[*e*,][1,2,4]triazin-4-yl, *J. Am. Chem. Soc.*, 2014, **136**, 11906–11909; (*c*) M. Fumanal, F. Mota, J. J. Novoa and J. Ribas-Arino, Unravelling the Key Driving Forces of the Spin Transition in π-Dimers of Spiro-biphenalenyl-Based Radicals, *J. Am. Chem. Soc.*, 2015, **137**, 12843–12855; (*d*) D.-H. Tuo, C. Chen, H. Ruan, Q.-Q. Wang, Y.-F. Ao, X. Wang and D.-X. Wang, Magnetic Multistability in an Anion-Radical Pimer, *Angew. Chem., Int. Ed.*, 2020, **59**, 14040–14043; (*e*) A. I. Taponen, A. Ayadi, M. K. Lahtinen, I. Oyarzabal, S. Bonhommeau, M. Rouzières, C. Mathonière, H. M. Tuononen, T. Clérac and A. Mailman, Room-Temperature Magnetic Bistability in a Salt of Organic Radical Ions, *J. Am. Chem. Soc.*, 2021, **143**, 15912–15917.

9 (*a*) H. Nishimaki and T. Ishida, Organic Two-Step Spin-Transition-Like Behavior in a Linear $S = 1$ Array: 3′-Methylbiphenyl-3,5-diyl Bis(*tert*-butylnitroxide) and Related Compounds, *J. Am. Chem. Soc.*, 2010, **132**, 9598–9599; (*b*) S. Matsumoto, T. Higashiyama, H. Akutsu and S. Nakatsuji, A Functional Nitroxide Radical Displaying Unique Thermochromism and Magnetic Phase Transition, *Angew. Chem., Int. Ed.*, 2011, **50**, 10879–10883; (*c*) T. Konno, H. Kudo and T. Ishida, Intermediate-paramagnetic phases with a half and a quarter spin entity in fluorinated biphenyl-3,5-diyl bis(*tert*-butyl nitroxides), *J. Mater. Chem. C*, 2015, **3**, 7813–7818; (*d*) A. Dragulescu-Andrasi, A. S. Filatov,

R. T. Oakley, X. Li, K. Lekin, A. Huq, C. Pak, S. M. Greer, J. McKay, M. Jo, J. Lengyel, I. Hung, E. Maradzike, A. E. DePrince III, S. A. Stoian, S. Hill, Y.-Y. Hu and M. Shatruk, Radical Dimerization in a Plastic Organic Crystal Leads to Structural and Magnetic Bistability with Wide Thermal Hysteresis, *J. Am. Chem. Soc.*, 2019, **141**, 17989–11994.

10 (*a*) A. Ueda, S. Yamada, T. Isono, H. Kamo, A. Nakao, R. Kumai, N. Nakao, Y. Murakami, K. Yamamoto, Y. Nishio and H. Mori, Hydrogen-Bond-Dynamics-Based Switching of Conductivity and Magnetism: A Phase Transition Caused by Deuterium and Electron Transfer in a Hydrogen-Bonded Purely Organic Conductor Crystal, *J. Am. Chem. Soc.*, 2014, **136**, 12184–12192; (*b*) T. Li, G. Tan, D. Shao, J. Li, Z. Zhang, Y. Song, Y. Sui, S. Chen, Y. Fang and X. Wang, Magnetic Bistability in a Discrete Organic Radical, *J. Am. Chem. Soc.*, 2016, **138**, 10092–10095.

11 A. Paul, A. Gupta and S. Konar, Magnetic Transition in Organic Radicals: The Crystal Engineering Aspects, *Cryst. Growth Des.*, 2021, **21**, 5473–5489.

12 (*a*) S. Hayami, Y. Shigeyoshi, M. Akita, K. Inoue, K. Kato, K. Osaka, M. Tanaka, R. Kawajiri, T. Mitani and Y. Maeda, Reverse Spin Transition Triggered by a Structural Phase Transition, *Angew. Chem., Int. Ed.*, 2005, **44**, 4899–4903; (*b*) R. Akiyoshi, R. Ohtani, L. F. Lindoy and S. Hayami, Spin crossover phenomena in long chain alkylated complexes, *Dalton Trans.*, 2021, **50**, 5065–5079; (*c*) T. Kanetomo, Z. Ni and M. Enomoto, Hydrogen-bonded cobalt(II)-organic framework: normal and reverse spin-crossover behaviours, *Dalton Trans.*, 2022, **51**, 5034–5040.

13 (*a*) D. Rosario-Amorin, P. Dechambenoit, A. Bentaleb, M. Rouziès, C. Mathonière and R. Clérac, Multistability at Room Temperature in a Bent-Shaped Spin-Crossover Complex Decorated with Long Alkyl Chains, *J. Am. Chem. Soc.*, 2018, **140**, 98–101; (*b*) F.-J. Valverde-Muñoz, M. Seredyuk, M. C. Muñoz, G. Molnár, Y. S. Bibik and J. A. Real, Thermochromic Meltable Materials with Reverse Spin Transition Controlled by Chemical Design, *Angew. Chem., Int. Ed.*, 2020, **59**, 18632–18638; (*c*) R. Kulmaczewski, F. Bamiduro, N. Shahid, O. Cespedes and M. A. Halcrow, Structural Transformations and Spin-Crossover in $[FeL_2]^{2+}$ Salts (*L*=4-{*tert*-Butylsulfanyl}-2,6-di{pyrazol-1-yl}pyridine): The Influence of Bulky Ligand Substituents, *Chem. – Eur. J.*, 2021, **27**, 2082–2092.

14 A. Paul, R. Nasani, A. Mondal, S. Roy, S. Vela and S. Konar, Reversible Magnetic Transition in a Bench-Stable Radical Cation Triggered by Structural Transition in the Magnetically Silent Counteranion, *Cryst. Growth Des.*, 2020, **20**, 6296–6301.

15 S. Koyama, Y. Horii, T. Sato, S. Takaishi, N. Hoshino, T. Akutagawa and H. Iguchi, Benzenetriimide-Based Molecular Conductor with Antiferro- to Ferromagnetic Switching Induced by Structural Change of π-stacked Array, *ChemPhysChem*, 2022, **23**, e202200322.

16 T. Kanetomo, K. Ichihashi, M. Enomoto and T. Ishida, Ground Triplet Spirobiradical: 2,2′,7,7′-Tetra(*tert*-butyl)-9,9′(10*H*,10′*H*)-spirobiacridine-10,10′-dioxyl, *Org. Lett.*, 2019, **21**, 3909–3912.

17 S. Ogawa, T. Kanetomo and M. Enomoto, Spiro-centre substitution effects in intramolecular spin-spin interactions of spirobiacridine diradicals, *Org. Chem. Front.*, 2024, **11**, 3004–3011.

18 G. M. Sheldrick, SHELXT – Integrated space-group and crystal structure determination, *Acta Crystallogr., Sect. A: Found. Adv.*, 2015, **71**, 3–8.

19 G. M. Sheldrick, Crystal structure refinement with SHELXL, *Acta Crystallogr., Sect. C: Struct. Chem.*, 2015, **71**, 3–8.

20 L. J. Bourhis, O. V. Dolomanov, R. J. Gildea, J. A. K. Howard and H. Puschmann, The anatomy of a comprehensive constrained, restrained refinement program for the modern computing environment – *Olex2* dissected, *Acta Crystallogr., Sect. A: Found. Adv.*, 2015, **71**, 59–75.

21 M. J. Frisch, *et al.*, *Gaussian09, Revision A.02*, Gaussian, Inc., Wallingford, CT, 2009.

22 Z. Liu, Q. Gao, J. Chen, J. Deng, K. Lin and X. Xing, Negative thermal expansion in molecular materials, *Chem. Commun.*, 2018, **54**, 5164–5176.

23 A. Bondi, van der Waals Volumes and Radii, *J. Phys. Chem.*, 1964, **68**, 441–451.

24 K. Yamaguchi, T. Kawakami, Y. Takano, Y. Kitagawa, Y. Yamashita and H. Fujita, Analytical and ab initio studies of effective exchange interactions, polyradical character, unpaired electron density, and information entropy in radical clusters (R)N: Allyl radical cluster (N=2–10) and hydrogen radical cluster (N=50), *J. Quantum Chem.*, 2002, **90**, 370–385.

25 H. M. McConnell, Ferromagnetism in Solid Free Radicals, *J. Chem. Phys.*, 1963, **39**, 1910.

26 K. Awaga, T. Sugano and M. Kinoshita, Ferromagnetic intermolecular interactions in a series of organic mixed crystals of galvinoxyl radical and its precursory closed shell compound, *J. Chem. Phys.*, 1986, **85**, 2211–2218.

27 T. Ishida, M. Ooishi, N. Ishii, H. Mori and T. Nogami, Mono- and dinitroxide radicals from 9,9′(10*H*,10′*H*)-spirobiacridine: An approach to a D_{2d} triplet biradical, *Polyhedron*, 2007, **26**, 1793–1799.

28 K. Ichihashi, T. Kanetomo, M. Enomoto and T. Ishida, 2,7-Di-*tert*-butyl-9,9′(10*H*,10′*H*)-spirobiacridine-10,10′-dioxyl as a ground triplet biradical: The role of *tert*-butylation, *Tetrahedron Lett.*, 2020, **61**, 152428.

29 T. Saito, A. Ito, T. Watanabe, T. Kawakami, M. Okumura and K. Yamaguchi, Performance of the coupled cluster and DFT methods for through-space magnetic interactions of nitroxide dimer, *Chem. Phys. Lett.*, 2012, **542**, 19–25.

30 (*a*) A. L. Allred and E. G. Rochow, A scale of electronegativity based on electrostatic force, *J. Inorg. Nucl. Chem.*, 1959, **5**, 264–268; (*b*) A. L. Allred, Electronegativity values from thermochemical data, *J. Inorg. Nucl. Chem.*, 1961, **17**, 215–221.

